

MHD Simulations of Relic Radio Bubbles in Clusters

T. W. Jones

Department of Astronomy, University of Minnesota, Minneapolis, MN 55455

twj@astro.umn.edu

D. S. De Young¹

National Optical Astronomy Observatories, Tucson, AZ 85719

deyoung@noao.edu

ABSTRACT

In order to better understand the origin and evolution of relic radio bubbles in clusters of galaxies, we report on an extensive set of 2D MHD simulations of hot buoyant bubbles evolving in a realistic intracluster medium. Our bubbles are inflated near the base of the ICM over a finite time interval from a region whose magnetic field is isolated from the ICM. We confirm both the early conjecture from linear analysis and the later results based on preformed MHD bubbles; namely, that very modest ICM magnetic fields can stabilize the rising bubbles against disruption by Rayleigh-Taylor and Kelvin-Helmholtz instabilities. We find in addition that amplification of the ambient fields as they stretch around the bubbles can be sufficient to protect the bubbles or their initial fragments even if the fields are initially much too weak to play a significant role early in the evolution of the bubbles. Indeed, even with initial fields less than a micro-Gauss and values of $\beta = P_g/P_b$ approaching 10^5 , magnetic stresses in our simulations eventually became large enough to influence the bubble evolution. Magnetic field influence also depends significantly on the geometry of the ICM field and on the topology of the field at the bubble/ICM interface. For example, reconnection of anti-parallel fields across the bubble top greatly reduced the ability of the magnetic field to inhibit disruptive instabilities. Our results confirm earlier estimates of 10^8 yr for relic radio bubble lifetimes and show that magnetic fields can account for the long term stability of these objects against disruption by surface instabilities. In addition these calculations show that lifting and mixing of the ambient ICM may be a critical function of field geometries in both the ICM and in the bubble interior.

¹ NOAO is operated by AURA, Inc. under contract to the National Science Foundation.

Subject headings: galaxy clusters – radio sources – MHD

1. Introduction and Motivation

Recent combined x-ray and radio observations of galaxy clusters have revealed a growing number of instances in which there is evidence on scales $\gtrsim 10$ kpc that extended radio sources produced by active galaxies in the cluster clearly displace the hot ambient intracluster medium (ICM), producing radio-filled, X-ray holes or “radio bubbles” (*e.g.*, Böhringer *et al.* 1993, Fabian *et al.* 2000, McNamara *et al.* 2001, Nulsen *et al.* 2002, Taylor *et al.* 2002, Blanton *et al.* 2004). Occasionally, as in the Perseus cluster, larger, apparently free floating radio quiet bubbles or “ghosts” are seen outside the inner radio structures (*e.g.*, Fabian *et al.* 2003). In several clusters an additional, remarkable phenomenon is observed; namely, apparent “relic” extended radio structures some tens of kpc from the central AGN with no apparent or at most faint radio connections between them (*e.g.*, Fujita *et al.* 2002, Mazzotta *et al.* 2002, Young *et al.* 2004). Together these various phenomena seem to infer that outflows from AGNs can inflate bubbles in the ICM, which then may dynamically evolve on their own during subsequent periods of reduced or absent energy outflow from the AGN. Recent observational summaries of these objects are given in Kempner *et al.* (2003) and Birzan *et al.* (2004). For simplicity we refer below to these isolated objects simply as relics¹ or bubbles.

In general the relic radio sources, and their more active inner companions, are smaller than classical FR-II objects, yet they often do not have the morphology that is characteristic of the lower powered FR-I radio sources (McNamara 2002). Typical radii of the relic radio bubbles are about 10 kpc, and their distances from the center of the parent galaxy range from about 20 kpc to 50 kpc. Thus these objects often lie in a transition region between the circum-galactic environment and the actual intracluster medium (ICM), a condition that will be addressed in more detail in §2. The radio luminosities of the relic bubbles lie in the lower end of that seen in the FR-I radio sources, while the luminosities of the inner components, when present, are comparable to those of FR-I objects.

A critical derived parameter for these objects is their estimated age. Age estimates for extended radio sources are notoriously uncertain (*e.g.*, De Young 2002), but in the case of the radio bubbles an age estimate can be obtained independently of the usual synchrotron lifetime

¹We do not address here another class of diffuse, “relic” radio sources in clusters, such as A3667, that may depend in part on large-scale shocks in current merger activity (*e.g.*, Roettiger *et al.* 1999) and that have recently been termed “radio gischt”, or “radio froth” (Kempner *et al.* 2003).

or Doppler boosting arguments. Because the radio bubbles displace the surrounding hot x-ray emitting gas, it can be argued that the density inside the bubbles is less than that of the surrounding medium, but that the interior gas is very energetic and in pressure equilibrium with the ambient gas. Under these conditions the bubbles will rise in the cluster gas as buoyant objects, and one can calculate the buoyant rise times of these objects from a point nearer the galaxy where the energetic material may have been injected. Such calculations have been done by e.g., Churazov et al 2001, and the resulting rise times are of order 10^8 yr. Similar results have been obtained by Birzan et al. (2004) from an examination of the observational data. While these calculations are also based upon several assumptions, it is interesting that the resulting ages for the relic bubbles are comparable to age estimates for radio sources obtained through the usual synchrotron aging arguments. However, if the radio bubbles are in pressure equilibrium with their surroundings, their internal energy densities exceed the synchrotron equipartition energy densities by about a factor of ten or more. This may have important consequences for the nature of the particle content of the radio bubbles and possible re-acceleration mechanisms (De Young 2003).

Given the above estimates for the parameters of the radio bubbles, a key issue immediately emerges. A clear observational result is that these objects are intact entities. Yet buoyant bubbles rising through a surrounding medium are unstable to fragmentation if the Reynolds numbers are at all large. This clearly should be the case here if hydrodynamic behavior is followed, since the hydrodynamic Reynolds numbers in this case are extremely large. Hence, the rising bubbles should quickly fragment due to both the Rayleigh-Taylor (R-T) and Kelvin-Helmholtz (K-H) instabilities along the top and sides of the bubble. Detailed numerical calculations have shown that this is in fact the case (e.g., Churazov et al. 2001, Brüggén et al. 2002). In particular, the detailed high-resolution simulations of Brüggén & Kaiser (2002) have shown that buoyant bubbles under conditions appropriate to the relic radio sources will become unstable and fragment into complex substructures in times of $\sim 10^7$ yr, which is much less than the estimated age of the observed relic radio bubbles. Hence in order to account for the observed data, some stabilization mechanism must be at work, and an obvious candidate is the intracluster magnetic field, perhaps in concert with the internal bubble magnetic field.

It has been known for some time that the hot gas in clusters of galaxies often has within it a significant magnetic field (e.g., Carilli & Taylor 2002, Taylor et al. 2002), with estimated typical magnetic field strengths of $\sim 5 \times 10^{-6}$ G (5μ G). It is also well known that magnetic fields can stabilize both the K-H and R-T instabilities (e.g, Chandrasekhar 1961; Shore 1992) if there is a significant field component that is parallel to the interface between the two fluids. The expansion of a radio source into an ambient medium that contains a tangled magnetic field will ensure that such tangential field components exist at the bubble-

ICM interface, independent of any magnetic field that is contained within the radio source itself. This stabilizing effect of intracluster magnetic fields was pointed out by De Young (2003) who derived analytic conditions for the stabilization of the relic radio bubbles in the hot ICM. Those calculations showed that the field strengths observed in many clusters will in fact stabilize the bubble interface in the linear regime, and hence the cluster magnetic fields could account for why the relic radio bubbles are seen as intact objects at such late times. Additional support for this idea is found in the two-dimensional MHD calculations of Brüggen and Kaiser (2001), who applied a $\beta \sim 10$ field inside the bubbles that was aligned with the bubble surface. Those calculations treated a scale much larger than that of the relic radio bubbles, covering regions 200 to 400 kpc in extent. Despite the large scales and the rather strong magnetic fields employed, the results are suggestive in that the radio source interface may be stabilized, and their resulting geometry is similar to that seen in the relic bubbles in clusters.

A more recent two-dimensional MHD study has been performed by Robinson *et al.* (2004) (hereafter R04). That work also addressed the evolution of relic radio sources in clusters, and it reported the results of both hydrodynamic and MHD calculations. The hydrodynamic results are very similar to those reported earlier, with the early onset of instability and subsequent fragmentation of the relic radio source bubbles. A basic result from R04 in the MHD case is that again the presence of even relatively weak magnetic fields can serve to stabilize the relic radio lobes as they rise in the ICM, which serves to verify the earlier considerations of magnetic effects mentioned above. The calculations of R04 were limited to two initial magnetic field configurations. One was a uniform magnetic field threading both the bubble and the ambient medium, the orientation of which was placed along each of the three principal axes in successive simulations. The other configuration involved a bubble supported against external gas pressure by an internal by force-free field. The ambient magnetic field in the computational plane was set to zero in that model, although it included a uniform field transverse to the computational plane that contributed (only) to the total pressure. Finally, R04 initialize their calculations with the bubble already in place, and assume a reflection symmetry across the vertical mid-line of the plane.

The new results described below are extensions of the work by R04 that are physically significant and immediately relevant to the evolution of relic radio bubbles in clusters of galaxies. They are still two dimensional. Like R04 we defer three dimensional simulations to follow-up work, since many 2D dynamical features remain qualitatively valid in 3D flows but are much easier to isolate and analyze in the 2D case. In contrast to the R04 simulations, the present calculations consider the effects of varying not only the ambient magnetic field orientation, but also its strength as a function of position. This provides a broader understanding of the roles played by the external magnetic field, permitting, for example,

the simulation of cluster atmospheres with constant $\beta = P_g/(8\pi B^2) = nkT/(8\pi B^2)$, which may be dynamically more likely in the intracluster environment. We also created our more general initial field configurations so that the bubble and external fields were isolated from one another, reflecting the distinct origins of the two fields. We also varied the topology of the field along the bubble/ICM interface, since that influences the magnetic reconnection expected there. In addition, while some of the R04 simulations were full MHD, those authors chose not to describe the behaviors of the magnetic fields in and around their bubbles, with the special exception of the one magnetically supported bubble. In addition, because the distance from the center of the parent galaxy to the relic radio bubbles is only a few tens of kiloparsecs, a realistic equilibrium ICM/ISM configuration is necessary that incorporates both the effect of the galaxy gravitational potential and that due to the inner regions of the cluster itself. Third, and perhaps most significantly, the present calculations differ from those of R04 in that we followed the dynamical evolution of radio bubbles as they were inflated and then evolve away from the source that supplies their internal energy. This is an essential element in determining realistic evolutionary tracks for the relic radio bubbles. The internal magnetic fields of the radio bubbles are evolved in a self consistent manner as the bubbles are inflated and then “cast off” into the ICM. Parameters for both the ambient ICM and the inflating bubbles are varied over a wide range in order to best determine which conditions may be most applicable to the cluster relic radio sources.

The plan of the paper is as follows. Section 2 describes the method of calculation used for these MHD simulations and a description of the initial and boundary conditions for the various cases considered. The results are presented in Section 3, together with an analysis of the physical processes at work. A summary and conclusions are presented in Section 4.

2. Calculation Details

Our simulations assumed 2D Cartesian geometry on the $y - z$ plane, with nonuniform gravity in the $-z$ direction, as outlined below. The computational domain was a square, 55 kpc on a side, spanning [5,60]kpc in z and centered on $y = 0$. Since radiative cooling is not important over the times simulated (see R04), we ignore that process and assign an adiabatic index, $\gamma = \frac{5}{3}$, to the compressible, conducting fluid. Further details of the ambient ICM are given below. The bubbles were inflated from a region of circular cross-section with radius $r_b = 2\text{kpc}$, centered at $y \approx 0$, $z = 15\text{kpc}$. Much of our study focuses on the evolution of instabilities that developed from irregularities on the surfaces of the expanding bubbles. Discrete mapping of the circular inflation region onto the Cartesian grid automatically creates seed perturbations for the instabilities. However, the simplest

mapping, with the inflation region centered at the intersection of grid-zone boundaries, introduces an artificial mirror symmetry into the simulation. To break that symmetry, and to “naturalize” the seed perturbations as much as possible, we applied two small modifications to the initial conditions. First, we offset the center of the inflation region in the y coordinate by $0.25\Delta y$, where $\Delta y = \Delta z$ is the size of a numerical zone. In addition, we added a 1% random noise to the ambient density distribution, providing a second, independent seed contribution of comparable amplitude to the mapping discretization. This noise was too small to have any other significant influence on the simulations. Other bubble creation details are presented below.

We used our well-tested ideal, compressible TVD ideal MHD code described in Ryu *et al.* 1998. The scheme is second order accurate in both space and time and is designed to capture cleanly all families of MHD discontinuities. It employs a constrained transport technique for updating the magnetic field, so that the initial divergence-free field condition is maintained to machine accuracy. This version of the code is $2\frac{1}{2}$ D, so that all three components of vector fields are included. However, the computations reported here all have $B_x = u_x = 0$. Both open z boundaries were designed to maintain hydrostatic equilibrium; the two y boundaries were open, as well. To track the bubbles we employed a passively advected mass-fraction tracer assigned value $C_f = 1$ for material originating inside the bubble inflation region, with $C_f = 0$ elsewhere. Simulations were carried out on grids ranging from 256^2 to 1024^2 . Only the two higher resolution cases are discussed here. Those resolutions are comparable to or exceed the stated effective AMR MHD resolutions of R04.

We add some brief general comments about considerations related to the finite numerical resolution involved in these simulations. Dissipation in our ideal MHD code results, of course, from approximation and roundoff errors rather than numerical models for those effects. Viscous and resistive dissipation are, thus, dependent on numerical resolution. Tests show that the effective kinetic and magnetic Reynolds numbers scale as $R \propto l^k$, where l is the scale of interest and k lies between 1.5 and 2, thus mimicking so-called “hyperviscosity” and “hyperresistivity” rather than normal viscosity and resistivity (*e.g.*, Ryu *et al.* 1995, Lee *et al.* 2003). On the other hand, while the physical viscosity and resistivity in collisionless astrophysical plasmas are not well-determined, they are unlikely to be expressible as simple, “normal-type” dissipation constants. In all the models run we found the results to be qualitatively independent of the three resolution used, since in all cases the effective kinetic and magnetic Reynolds numbers on scales that dominate the dynamics (more than a few zones) exceed several hundred. That consistency agrees with our earlier resolution studies with this code (*e.g.*, Jones *et al.* 1996, Miniati *et al.* 1999). While the fine details of the observed behaviors do depend on numerical resolution for several reasons, our aims here are more general and not significantly impacted by resolution effects. A specific note about magnetic

reconnection is also warranted in this regard. Reconnection is a topological transformation of the magnetic field that requires dissipation in order to take place. While details of that transformation certainly depend on the details of the dissipation, previous 2D and 3D numerical studies with this code have found that global behaviors are once again consistently obtained once the magnetic Reynolds numbers become large (*e.g.*, Jones *et al.* 1997, Ryu *et al.* 2000).

2.1. The Gravitational Potential and Ambient Medium

Because the observed relic radio bubbles lie $\sim 20 - 50$ kpc from the nuclei of the parent galaxies, the buoyant bubbles of interest rise in an environment that is influenced by both the mass contained in the cluster core and that of the parent galaxy. Hence, the gravitational potential used in our simulations is a superposition of those due to both the cluster and the active galaxy. Observational data that supply kinematic verification of such models are rather scarce, but this problem has been treated in a different context by Kelson *et al.* (2002). The present calculation follows their approach. The mass distribution in the cluster core, including dark matter, follows an NFW model (Navarro, Frenk & White 1997) with a total density distribution given by $\rho_c(\zeta_c) \propto 1/[\zeta_c^\alpha(1 + \zeta_c)^{3-\alpha}]$, where ζ_c is a normalized cluster radius; $\zeta_c = r/r_s$. Several choices are available for modeling the mass distribution of the parent galaxy, such as an $r^{1/4}$ law, a “King” model (King 1966, 1978), or another power law distribution. Kelson *et al.* found that the observational data in the inner regions were relatively insensitive to the model chosen for the galaxy mass distribution, and hence we chose an easily integrated King model of the form $\rho_g(\zeta_g) = \rho_o/[1 + \zeta_g^2]^{3/2}$, where $\zeta_g = r/a$. This gives $M(\zeta_g) = 3M_c[\ln(\zeta_g + \sqrt{1 + \zeta_g^2}) - \zeta_g/\sqrt{1 + \zeta_g^2}]$, where, a is the core radius of the galaxy and M_c is the core mass.

In our simulations we assumed an NFW cluster model with $\alpha = 0$, $r_s = 400$ kpc, and a normalization of $M_{cluster} = 3.5 \times 10^{10} M_\odot$ at 10 kpc. This yields a cluster mass of $3.5 \times 10^{12} M_\odot$ at 50 kpc. For the galaxy, a core radius of $a = 3$ kpc was chosen, normalized to a galaxy mass of $3.5 \times 10^{12} M_\odot$ at a radius of 20 kpc. With this model, the equal mass contribution crossover point occurs at a radius of about 60 kpc. The total and constituent mass distribution, along with the radial gravitational acceleration are shown in Figure 1. Since our simulations were carried out on a Cartesian grid, we substituted the z coordinate for r , and will henceforth use z to indicate vertical distance.

Again applying a Cartesian geometry, we took the ICM to be an isothermal plane stratified hydrostatic atmosphere with $kT = 3$ keV ($T \approx 3.5 \times 10^7$ K) and a hydrogen mass fraction $X = 0.75$ (mean molecular weight, $\mu \approx 0.6$), yielding an ICM adiabatic sound speed

$c_{sI} = \sqrt{(\gamma P/\rho)} = 0.914 \text{ kpc/Myr} = 894 \text{ km/sec}$. (Henceforth, we shall use the subscript “I” to indicate ICM initial conditions.) An electron density in the atmosphere set to $n_e = 0.1 \text{ cm}^{-3}$ at $z = 5 \text{ kpc}$ leads to the density and pressure distributions shown in Figure 1. The ICM scale height, which we can define to be $h = c_{sI}^2/|g|$, increases roughly linearly from $h \approx 5 \text{ kpc}$ at the bottom of our computational domain to $h = 57 \text{ kpc}$ at the top. That is, $h \approx z$. This behavior allows us to derive a simple and useful form for the variation of the pressure and density with height. In fact, it is easy to show that $P \approx P_0(z/z_0)^{-\gamma}$, with a similar form for density. We have verified this to be a good fit to the actual ICM profiles.

The initial magnetic fields of the ICM and the bubble were isolated from one another. The ambient field was generated from a magnetic stream function, A_x , given in polar coordinates with respect to the bubble injection center as $A_x = B_0 \sin(\phi - \phi_0)(1 - (r_b/r)^2)$ for $r > r_b$, where ϕ and ϕ_0 are measured from the y -direction, and r_b is the radius of the bubble inflation region. ϕ_0 rotates the field structure around the bubble injection center, to allow an arbitrary orientation. The magnetic field components are $B_r = B_0 \cos(\phi - \phi_0)(1 - (r_b/r)^2)$ and $B_\phi = -B_0 \sin(\phi - \phi_0)(1 + (r_b/r)^2)$. For $\phi_0 = 0$ this becomes a uniform horizontal field ($B_z = 0$, $B_y = B_0$) as $r \rightarrow \infty$. As $r \rightarrow r_b+$, $B_r \rightarrow 0$, so that the field becomes tangential to the bubble inflation region, with a peak magnitude equal to $2B_0$. Initial ambient fields defined by A_x alone are identified below as “uniform” or “U”, since away from the bubble they are nearly so. For the simulations discussed below $B_0 > 0$. We carried out “uniform” field simulations with $\phi_0 = 0^\circ, -45^\circ, -90^\circ$, although we omit discussion of uniform fields with $\phi_0 = 0^\circ$ and $\phi_0 = -90^\circ$, since they are very close in behavior to the analogous models described in R04.

In addition we computed $\phi_0 = 0$ models, designated below as “constant β_I ” or “B”. There we modified the magnetic field found from A_x and the gas pressure illustrated in Figure 1 so that $P(z) \rightarrow P(z)\beta_I/(1 + \beta_I)$ with $2P/B_y^2(y \rightarrow \infty) = \beta_I$, where P is the gas pressure. This maintains hydrostatic equilibrium in the z -direction with an almost constant β_I . By rescaling the “U” model B_y in proportion to $\sqrt{P(z)}$ and applying a small correction to B_z it is possible in this model to maintain the divergence-free condition in the initial ICM field. The smallest β_I modeled was 120, so equilibrium in the y -direction was not significantly disturbed by this procedure.

2.2. Bubble Inflation and Magnetic Field

At the start of each simulation the “bubble inflation” region was established and maintained for a time t_i that ranged over $0 \leq t_i \leq t_e$, where t_e was the end time of the simulation. The bubble inflation region had a radius $r_b = 2 \text{ kpc}$, centered at $z = 15 \text{ kpc}$, and it was given

a density equal to 1% of the ambient density of the ICM at $z = 15$ kpc. We gave the inflation region constant pressure, matching the ambient pressure at $z = 15$ kpc. The associated sound speed internal to the bubble, c_{sb} , consequently exceeded that of the ICM by a factor of ten. The uniform pressure inside the inflation region resulted in a slight, 10% gas overpressure compared to that of the ambient medium on the upper boundary of the inflation region, which led to a brief, dynamically insignificant spike in the initial energy flux into the bubbles. The inflating bubbles expanded subsonically with a density comparable to the inflation region. They were lifted upward by buoyancy with a velocity $\sim 0.2 - 0.6c_{sI}$ as discussed in §3.1. The bubble inflation power, defined as the total energy flux across the boundary of the inflation region, is given by $\dot{E}_b = \oint ds u_i (\frac{5}{2}P_i + P_{bi} + \frac{1}{2}\rho_i u_i^2)$, where P_i , P_{bi} , ρ_i and u_i represent the gas pressure, magnetic pressure, gas density and radial outflow velocity at the boundary of the inflation region, respectively. Since the pressure and density inside the inflation region remained fixed during the inflation interval, \dot{E}_b was controlled by u_i , which was always small compared to the internal bubble sound speed, c_{sb} . Therefore, since the Poynting flux is also generally negligible, $\dot{E}_b \approx 2\pi r_b u_i \frac{5}{2}P_I$. Outflow speeds into the inflating bubbles mirrored, in fact, the upward buoyant bubble expansion. Thus, since this leads to $u_i \lesssim 0.5c_{sI} \lesssim 0.05c_{sb}$, \dot{E}_b typically increased at the start of the simulations towards $\sim 10\%$ of the characteristic value, $\dot{E}_0 = 2\pi r_b P_I c_{sb}$. If the inflation region was maintained longer than the time required for the inflating bubble to rise through one ICM scale height ($\propto h/c_{sI}$), typically about 20 Myr in these simulations, a crude de Laval nozzle formed about one scale height above the inflation region. In such cases a collimated, transonic to mildly supersonic flow continued higher into the ICM so long as the inflation was maintained. That plume was capped by a bubble, analogous to the flows simulated by Brüggén & Kaiser (2002).

A circumferential magnetic field was imposed inside the active inflation region, given by $B_r = 0$, $B_\phi = B_1(r/r'_b)$, for $r \leq r'_b = r_b - 4\Delta z$, then decreased quadratically to zero at $r = r_b$ in order to isolate the bubble magnetic field, initially. In the models discussed $|B_1| = 2|B_0|$, in order to match the peak perimeter field in the “U” models. The same ratio was used in the “B” models. In that case, the ambient field strength varies asymmetrically across the bubble, so there is no simple match in the internal and external field strengths. On the other hand, in both types of models, the magnetic field inside the bubble is strongly modified by flow, especially shear, so these details are not very significant. During the inflation period, magnetic fields advected from the inflation region were lifted into the rising bubble and stretched around the interior perimeter, enhancing the magnetic field just inside portions of the side and bottom boundaries by as much as a factor of two, which is qualitatively an expected result. In most cases B_1 was positive, giving a counterclockwise sense to the initial bubble field. Then the internal and ambient fields were parallel at the bottom of the bubble and anti-parallel at the top when $\phi_0 = 0^\circ$. For the two cases identified below by the letter

“R”, the internal field was reversed with respect to this convention.

We note that the initial magnetic field configurations are divergence free everywhere. This is clearly true inside the bubble inflation region and outside, as well. A little thought shows that it is also true across the boundary between them. The key point is that no magnetic flux crosses that boundary. Thus, an accounting of the flux through a cylindrical test shell including that boundary can be separated into two independent parts with the boundary dividing them. Each piece separately has zero net flux, so the full test box does, as well.

3. Discussion

We carried out a total of 28 model simulations, varying the magnetic field geometry and strength, its topology along the bubble boundary, the time for which bubble inflation was maintained, as well as the numerical resolutions used. We included models with “preformed” bubbles ($t_i = 0$) in uniform ambient magnetic fields that were both horizontal ($\phi_0 = 0^\circ$) and vertical ($\phi_0 = -90^\circ$) in order to mimic the kinds of models studied in R04. Those simulation behaviors resemble qualitatively the results reported in R04 for similar bubbles, confirming their results. We will not discuss them here. Rather, in order to extend our understanding, we focus instead on ten representative simulations that involved nonuniform horizontal or uniform oblique ambient fields ($\phi_0 = -45^\circ$), with finite periods for inflation of the buoyant bubble plasma. Table 1 summarizes their properties.

3.1. Bubble Energetics and Buoyant Dynamics

Our main objective is to understand better the roles of magnetic fields in the bubble dynamics. However, before examining the specific influences of magnetic fields, it is helpful to look briefly at the general energetic and dynamical behaviors of the bubbles in the modeled ICM environment. For instance, the evolution of instabilities, magnetic fields and circum-bubble flows depends on the history of bubble motions. Hence, this section provides a brief overview of how bubble inflation evolves, and it describes evolutionary features that are common to many of the simulations that were performed. This background will assist in understanding the subsequent discussion of the evolution of specific models calculated. Figures 2 and 3 provide representative examples of the evolution of the bubble energy contents and volume for very different energy injection times. Figure 2 illustrates model BM_h (horizontal magnetic field with constant β), $t_i = 10$ Myr. Other behavior of this model, to be discussed

below, can be seen in Figure 8. As explained already in §2.2, the bubble inflation power, \dot{E}_b increased through the inflation period as the bubble accelerates its expansion into the ICM. The total energy injected (per kpc in the third, x direction) was about 6.4×10^{56} erg. For convenience, length, time and energy in the figures are expressed in natural units of the simulations, with time in Myr, length in kpc and mass corresponding to ICM inside 1 kpc^3 . The natural energy unit then becomes, $E_0 = 5.5 \times 10^{55}$ erg.

At the end of the inflation period, the 2D bubble volume, $V_{bub} \sim 28 \text{ kpc}^2$, so a characteristic radius of the bubble is $R \sim \sqrt{V_{bub}/\pi} \sim 3 \text{ kpc}$. As the bubble subsequently expanded adiabatically, its volume increased by a factor ≈ 2.7 relative to the value at the end of the inflation period, while the total energy inside the bubble dropped by a factor $\approx (1/2.7)^{2/3} = 0.52$ as one would then expect. In this case, as in all the others we computed, the total energy in the bubble was dominated by thermal energy. We note that the spike in the kinetic energy seen at $t = t_i$ corresponds to termination of the bubble inflation. At that moment conditions inside the inflation region were no longer held fixed, so that the inflation region was effectively “released” into the ICM. It was buoyant, of course, so it briefly surged upward within the bubble.

It is worth mentioning the evolution of magnetic energy inside the bubble, illustrated in Figure 2. Even though the bubble thermal energy decreased as expected during expansion, the bubble magnetic energy increased, albeit irregularly. A purely toroidal field, B_ϕ would have decreased inversely with the radius of the expanding bubble in order to satisfy magnetic flux conservation. Alternatively, a fully disordered field in 2D would decrease as $\sqrt{\rho}$ during bubble expansion. Either condition would have lead to a constant bubble magnetic energy in 2D. The observed global increase in the bubble magnetic energy was a manifestation of strong, organized internal bubble mass circulations, also associated with some of the irregularities in bubble kinetic energy content.

Figure 3 provides similar energetics information for model BS-C, which has the same geometry as the above case but a lower value of β . In this case the bubble inflation region was maintained for the full 65 Myr of the simulation, by which time the bubble approached the top of the grid. Figure 11 illustrates the general appearance of the bubble in this model. The bubble inflation power, \dot{E}_b , reached an approximate steady state $\sim 2.6 E_0/\text{Myr} = 1.7 \times 10^{42}$ erg/sec/kpc after 20 Myr, which corresponds to the formation epoch of the de Laval nozzle near $z \approx 25$ kpc. We confirmed that the flow was transonic at that location with $v \approx c_s \sim 3 - 4 c_{sI}$. The total energy flux through the nozzle closely matched the inflation energy flux seen in Figure 3. Fluctuations seen in the latter quantity resulted from instabilities in the flow near the nozzle. Smith *et al.* (1983) pointed out that there should be a critical energy flux for bubble inflation, which in our 2D Cartesian geometry would be

$\dot{E}_c \approx P_I c_I h$. Below this energy flux the de Laval nozzle is expected to pinch off the flows, so that they are unsteady, while above this energy flux steady flows can be maintained. For our conditions, $\dot{E}_c \approx 1.5 E_0 / \text{Myr}$, or about 57% of the inflation kinetic energy flux that developed in this simulation.

The overall evolution of bubbles in the ICM under these two extremes of energy injection times proceeded much as expected from intuition. The status of continuing physical connections between real cluster radio bubbles and their parent AGNs is not unambiguous. Almost by definition these objects do not display radio loud, jet AGN connections, so it is simplest to assume that they are independent. It may be premature to draw that conclusion generally, however, since faint radio bridges have been seen in a couple of cases (MKW3S and A133, Young *et al.* 2004). We leave that issue open for now.

Some additional key properties of bubble dynamics can also be gleaned from Figures 4, 5 and 6. Figure 4 illustrates the buoyant motions of several models. The upper panel plots the position of the top of each bubble shown, where z_{top} is defined as the highest point at which the bubble mass-fraction tracer $C_f \geq 0.95$. The center panel plots the mean height of each bubble, defined as $z_{bub} = (\int z C_f dydz) / (\int C_f dydz)$. The bottom panel shows the mean upward velocity of each bubble, defined as $v_z = d(z_{bub})/dt$. Except for model BS-C, which has ongoing inflation, all the models shown have the same short inflation period; namely, $t_i = 10$ Myr. The v_z spikes at $t = t_i$ are caused by the upward surging lower boundary of the bubble as it is released. As we shall see, the various bubble models have rather different stability behaviors, morphologies and internal dynamics. Nonetheless, except for BS-C, their buoyant upward motions through the ICM are qualitatively similar.

On the other hand, stability and circum-bubble flows depend essentially on the upward bubble velocity and also on the bubble acceleration. To facilitate the relevant discussion it is helpful to derive the usual expression for bubble terminal velocity, which is, of course, determined by a balance between buoyancy and drag. The general expression of the buoyant force is

$$F_{buoy} = - \int g C_f (\rho_I - \rho) dydz. \quad (1)$$

Substituting $-g = c_{sI}^2/h$, assuming a constant ICM sound speed and that the bubble density is small compared to the ICM, this can be approximated in a convenient form

$$F_{buoy} \approx c_{sI}^2 \langle \rho_I / h \rangle V_{bub}, \quad (2)$$

where the angular brackets represent an average over the bubble volume, V_{bub} . The drag force can be expressed as

$$F_d = C_d L_y \rho_I (z_{top}) v_z^2, \quad (3)$$

where C_d is a drag coefficient, $\rho_I(z_{top})$ indicates the ICM density at z_{top} and L_y measures the horizontal width of the bubble. Then the expected terminal velocity is

$$v_t = \sqrt{\frac{F_{buoy}}{C_d L_y \rho_I(z_{top})}}. \quad (4)$$

Figure 5 compares v_z (solid lines) for four model bubbles with v_t found from equation 4 using equation 2 for F_{buoy} (dashed curves). Here L_y was set at each time to the maximum y extent of the bubble gas, and it was assumed that $C_d = 2$ in each case. The simple, “universal” model, with constant C_d , represents the motions of all the bubbles remarkably well. Obvious variances between the model and the BS_h and BS-R simulations late in the simulations resulted from MHD effects, as will be discussed in §3.2.

The most important property of measured bubble motion after release was that it generally decelerated. That resulted simply from the fact that the scale height of the ICM increased with z , which, in turn, resulted from the decreasing gravity. We can see this simply from equation 5 if we approximate the bubble cross section as a cylinder, so that $L_y = \sqrt{4V_{bub}/\pi}$. Since $V_{bub} \propto P_I^{-3/5}$, and we pointed out in §2.1 the approximate ICM behavior $P_I \propto z^{5/3}$, we expect from equation 5 that $v_z \propto z^{-1/4}$, roughly consistent with the numerical results. This decelerated upward motion reduced both the sheared flows around the bubbles and the strength of vortical motions over time as they rose. That, in turn reduced disruptive instabilities and the ability of the bubbles to lift ICM in their wakes.

Representative examples of the velocity fields found in association with the bubbles can be seen in Figure 6. The figure illustrates the flows at the end of four simulations with short injection periods, $t_i = 10$ Myr. In each case ambient, ICM gas has been lifted in response to vortical structures developed early on along the sides of the bubbles. As the vortical flows weakened and separated, returning “down drafts” developed underneath the bubble centers, as can be seen in the figure. ICM was also pushed upward above the bubble tops, especially in models with strong magnetic fields. Circulations developed within the bubbles, as well. Their strength depends on the strength and geometry of the magnetic fields within the bubbles as we shall discuss in the following subsection.

We comment that it is not reliable to use simulations with such limited spatial domains to examine quantitatively the redistribution of energy and entropy within the overall ICM (*e.g.*, Brüggén & Kaiser 2002), since energy and gas do cross the outer boundaries of the computational domain. This effect will influence the large scale flows and modify the bulk transport of quantities.

3.2. The Influence of Magnetic Field Strength and Geometry

We begin our discussion of the influence of magnetic fields with some brief general reminders about the instabilities that largely determine the survivability of the bubbles, starting with the Rayleigh-Taylor (R-T) instability. The top center of a bubble is subject to the R-T instability, especially early on, when the local gravity is relatively stronger. This will lead to dense fingers of the ICM penetrating into the bubble from above. A tangential magnetic field can stabilize the R-T instability (Chandrasekhar 1961) if the restoring tension generated by bending of the field lines exceeds the buoyancy force driving the instability. In the limit that the ICM density greatly exceeds the bubble density and the magnetic field strength continues across the contact discontinuity the linear stabilizing condition can be expressed approximately in terms of the MHD β parameter as $\beta < \beta_{crit} \approx 8\pi h/\gamma\lambda$, where λ is the wavelength of the perturbation along the boundary (Jun & Norman 1995). Thus, the R-T instability is inhibited for small-scale surface perturbations of wavelength $\lambda_{kpc} \lesssim 25h_{kpc}/\beta$, where h_{10kpc} expresses the scale height in kiloparsecs. In our simulations $h_{kpc} \approx 10$ where the bubbles form, while initial β s range from $\beta \sim 10^2 - 10^5$. In the weak field cases with $\beta > 10^3$, perturbations should initially be R-T unstable down to scales well below the size of the bubble. On the other hand, we may expect the strong field cases, with $\beta \sim 10^2$, to be R-T stable. These theoretical expectations are confirmed in the simulations as discussed below.

Disruptive Kelvin-Helmholtz (K-H) instabilities may develop in response to strong shear along the outer boundary of the bubbles once they start to rise, when the ICM flows around them and strong vortices form along the bubbles in their wakes. In addition, circulation developed inside the bubbles that contributed strong shear at the bubble boundary. The strength and location of shear on the bubble boundaries varied with time and with the magnetic field properties. Those details aside for the moment, we find from inspection that tangential velocity differences across the bubble boundary were commonly as large as $\sim 0.2 - 0.4$ kpc/Myr (that is, $\lesssim 0.5c_{sI}$) over much of the simulation time intervals, even when the upward motion of the bubbles became less than this late in the simulations (see Figures 4, 5). The relatively large shear rates resulted in part because the internal flow speed coming from circulation within the bubble can be larger than the instantaneous upward speed of the bubble.

Tangential magnetic fields can inhibit the K-H instability if the restoring magnetic tension induced by bending the field lines exceeds the local “Bernoulli lift force” due to flows over boundary corrugations. Formally, the instability is inhibited if the “rms” Alfvén speed across the boundary, $v_{A_{bnd}}$ (defined as $v_{A_{bnd}}^2 = (B_1^2 + B_2^2)/(4\pi)(1/\rho_1 + 1/\rho_2)$), exceeds the velocity difference across the boundary (Chandrasekhar 1961; Vikhlinin *et al.* 2001). Since at

the start of our simulations, the magnetic field just inside the bubble boundary was typically at least as large as that immediately outside, but the gas density was lower by two orders of magnitude, $v_{A_{bnd}}$ was initially close to the Alfvén speed just inside the bubble boundary.

For discussion it is helpful to express v_A in terms of the sound speed and β ; namely, $v_A = \sqrt{\frac{6}{5}}c_s/\sqrt{\beta}$. Using this expression it is apparent that v_A in the ICM was from one to two and a half orders of magnitude smaller than the ICM sound speed for the models listed in Table 1. At the same time, the bubble sound speed was larger by an order of magnitude than c_{sI} , while β inside the bubble perimeter was initially smaller by about an order of magnitude. Together, these produced an internal $v_A \sim v_{A_{bnd}}$ that initially ranged from being an order of magnitude smaller than c_{sI} in the weak field models to being comparable to c_{sI} . Since the tangential velocity jumped across the bubble boundaries approached a substantial fraction of c_{sI} as the bubble started to rise, we expect the K-H instability to be operative initially in the weak-field cases, but not in the strongest field cases. That is confirmed by the simulation behaviors. The role of the internal magnetic field in more evolved bubbles varies, depending on the strength and configuration of the initial field, as discussed below.

3.2.1. Short Bubble Inflation Periods

General features of the evolutionary histories of three bubbles with an inflation period, $t_i = 10$ Myr are illustrated² in Figures 7, 8 and 9. The images show magnetic pressure and gas density structures for bubbles inflated in constant β_I atmospheres with $\beta_I = 75550$, 3000, and 120. The associated ambient field values at $z = 30$ kpc are 0.2, 1, and 5 μG , respectively. Near the base of the atmosphere the ambient field was roughly four times the value at $z = 30$ kpc, while it dropped to about half that value near the top of the computed region. The bubble plasma (as established by $C_f \approx 1$) was closely coincident with the darkest tones in the density images. This provides a relatively easy way to follow evolution of the bubbles. In particular, their integrity can be ascertained by examining continuity of dark structures. At $t = 150$ Myr the density distributions in Figures 7, 8, 9 and 10 can be directly compared to the mass-fraction contours in Figure 6.

The weakest field case (model BW, Figure 7) with $\beta_I = 75550$, corresponding to ICM fields of a few tenths of a μG , evolves almost, but not quite, hydrodynamically. Thus, as expected, the bubble was completely disrupted into fragments by R-T and K-H instabilities soon after its inflation ended, and before it could rise significantly above the inflation region.

²mpeg animations of these quantities can be found at <http://www.msi.umn.edu/Projects/twj/newsite/projects/bubbles/>

One can see evidence of the R-T instability along the bubble top and the K-T instability on the sides in the $t = 12.5\text{Myr}$ density image. By $t = 75\text{Myr}$ the bubble was largely twisted and stretched into several barely connected fragments. Eventually, even in this case, magnetic fields played a stabilizing role in the behavior of bubble fragments, but too late to save the original bubble. The magnetic pressures illustrated in Figure 7 reveal that ICM magnetic fields became wrapped around and stretched between the bubble fragments. Generally, the field lines aligned with the most intense field structures, so the highlighted features in the images approximately illustrate the field topology in intense field regions, as well. In this case fields were amplified locally to as much as several μG , corresponding to Alfvén speeds, $v_A \sim 0.2 \text{ kpc/Myr}$, which are comparable to the maximum velocity jumps found. Magnetic reconnection induced by circulation within the larger bubble fragments reduced the internal field after some initial amplification due to stretching. Consequently, the enhanced ICM field was dynamically more important than the internal field during later stages of the simulation.

Because the early evolution was essentially hydrodynamical, the behavior of this bubble is qualitatively similar to the hydrodynamical bubble shown in Figure 1 of R04. The most apparent difference between the density distributions of the two simulations is the left-right mirror symmetry in the R04 bubble, contrasting with the asymmetric evolution of our BW bubble (resulting from small breaks in the symmetry of the initial conditions) that make its morphology more irregular.

A curious magnetic feature formed late in the evolution of this bubble model as well as in all others we have carried out that terminate bubble inflation well before the end of the simulation. This feature is most obvious in the $t = 150\text{Myr}$ magnetic pressure image of Figure 7, where magnetic sheets can be seen extending down below the bubble material and folding over one another near the base of the ICM. Analogous features can be seen in Figures 8 and 9. This magnetic structure formed as magnetic fields were stretched inside the downdraft that forms as the upward motion of the bubbles decelerated. Counter-rotating vortices that developed initially along the perimeters of the rising bubbles dragged ICM material upward in the bubble wakes and formed a current sheet near the center-line of the wake. This can be seen in the velocity fields of Figure 6. As the upward motion of the bubbles decelerated, these vortical patterns weakened and separated, allowing ICM material directly underneath the bubble to settle again, depositing the paired sheets of oppositely directed ambient magnetic field separated by a thin current sheet. The folded sheets were in the process of annihilating through reconnection, but that rate was roughly matched by the deposition rates in the simulations.

The model BM_h ($\beta_I = 3000$) illustrated in Figure 8 also began its evolution almost hydrodynamically. Once again, R-T and K-H instabilities were clearly in evidence during

the early evolution, while strong vortices developed along the bubble sides that incorporated significant bubble plasma. The bubble plasma inside these two lateral vortices was eventually shed from the main bubble mass. However, both external and internal magnetic fields were quickly strengthened as the bubble inflated and began to rise. External field was pushed up with the rising bubble, then stretched and amplified around the bubble and wrapped into the vortices. Inside the rising bubble an additional pair of counter-rotating vortices formed during inflation that stretch the internal magnetic fields into intensified flux sheets along the bubble walls. This further inhibited R-T and K-H instabilities on the bubble perimeter. Near the top center, however, it is also evident in the $t = 75\text{Myr}$ images that the bubble was bifurcated by a dominant R-T finger formed near the center of the bubble top. So, in this location, the R-T instability continued. This behavior resulted from the initial magnetic reversal between the ICM and bubble fields on top of the bubble combined with the effects of internal bubble motions. The initially anti-parallel fields on the bubble top reconnected in this vicinity. In addition, the internal counter-rotating vortices deformed the internal magnetic field near the bubble top into anti-parallel sheets that also reconnected (see, for example the magnetic pressure images at $t = 12.5\text{Myr}$ in Figures 7 and 8). Consequently, the magnetic field was locally much reduced compared to the rest of bubble perimeter, and this allowed the R-T instability to continue in this area into the nonlinear phase.

To explore further the above physics behind the bifurcation of the B1-H bubble, we carried out a complimentary pair of simulations at half the resolution of BM_h . The first of these, BM, was identical to BM_h except for the lower resolution and behaved in a fashion very consistent with the higher resolution case just described. The other simulation, BM-R, was identical to BM except that the initial bubble magnetic field was reversed, so that it was parallel to the external field on the bubble top, but anti-parallel on the bubble bottom. As expected from the previous discussion, the bubble in BM-R was not disrupted. Except for the shed lateral vortices, which became magnetically isolated from the main bubble body, it remained intact, since the initial instabilities were quenched by magnetic tensions over the entire top portion of the bubble. The same pair of internal vortices developed in the BM-R bubble, and their motions still reduced the field inside the bubble top. However, the amplified external field was strong enough to inhibit nonlinear growth of the R-T instability. In fact, as the upward motion of the bubble decelerated the main bubble body developed a quasi-circular cross section in response to the external magnetic hoop stresses.

After release from the inflation region, internal bubble circulations in the BM bubbles amplified the field just inside the bubble wall until the local Alfvénic Mach number was of order unity, thus damping the circulation there at later times. Deeper inside the bubble fragments, however, circulation annihilated much of the magnetic field, so the motions continued. By about $t \sim 40\text{Myr}$ K-H instabilities were largely inhibited by the strengthening

surface field, although the R-T finger formed early on continued to develop. The magnetic field on both sides of the top bubble surface intensified to values as large as $20 \mu\text{G}$ as the bubbles rose, so that Alfvén speeds approached c_{sI} and $\beta \rightarrow 10$.

The bubble in the stronger ambient field simulation, BS_h , ($\beta_I = 120$; Figure 9) was mostly stable against R-T and K-H instabilities from the very start, as predicted in our simple analysis at the start of §3.2. The bubble remained intact. On the other hand, just as for the BM and BM_h models, the magnetic field of the bubble and the ICM were anti-parallel on the bubble top and sides. There was significant reconnection in these regions as the bubble started to push upward. Similar to the BM cases, this produced a noticeably weakened magnetic field along the top and sides of the bubble. On the other hand, the internal magnetic field quickly became strong enough to inhibit formation of the internal, vortex pair seen in the BM bubbles. This resulted in little internal magnetic reconnection, and the R-T instability on the bubble top never developed. However, a lateral vortex pair did form out of the K-H instability on the trailing edges of this bubble, similar to the BM bubbles. In this case, however, the magnetic field stretched inside those vortices quickly became large enough to distort and disrupt the vortex flow. The local Alfvénic Mach number there dropped to near unity, as did β . Previous MHD studies of the 2D K-H instability have shown that such evolution leads to distended vortices similar to those visible in Figure 9 (Jones *et al.* 1997). Eventually, the lateral vortices were pulled into the main bubble structure, squeezing it laterally and actually accelerating its mean upward motion. Magnetic fields on the top of bubble reached values almost an order of magnitude larger than the initial field surrounding the bubble. The Alfvén speed on both sides of the bubble boundary and deep into the bubble interior approached c_{sI} , so that the magnetic fields played a very important role in the motions of the bubble and in the circulations within the bubble. In particular, the magnetic hoop stress at the bubble top, $F_M \sim v_A^2 \rho / R$, where R is the bubble radius, became comparable to the buoyancy force per unit volume, $F_{buoy} \sim \rho_I |g| \sim c_s^2 \rho_I / h$. Their ratio is $F_M / F_{buoy} \sim (v_A^2 / c_s^2)(h/R)$. We pointed out that $v_A \sim c_{sI}$. Since $R \sim h$, this ratio was close to unity. In fact the upward motion of the BS_h bubble almost stalled before the body of the bubble was briefly thrust upward after $t \sim 110 \text{ Myr}$ by the previously mentioned interaction with the lateral vortices (see Figure 5).

The BS_h model (Figure 10) provides another example of the possible importance of the magnetic field topology to the bubble dynamics. This model is identical to BS_h except that it has half the numerical resolution and the bubble magnetic field is reversed to make it parallel with the ICM magnetic field on the bubble top. Thus, it represents a stronger-field comparison test similar to the one already discussed for the BM simulations. Consequently, the only reconnection between the bubble and ICM fields took place very near the bottom of the bubble at the start of the simulation. Hence, the bubble magnetic field remained

largely isolated from the ambient ICM field. The K-H instability was completely inhibited, so no vortical motions developed that involve both bubble and ICM plasma. The bubble remained intact, and β within the bubble dropped to values as low as two by the end of the simulation. The internal magnetic fields became well-ordered, looping neatly parallel to the external bubble boundary, since internal bubble circulation was largely damped out. The external magnetic field decelerated the upward motion of the bubble, similarly to model BS_h (or the lower resolution equivalent, BS). However, the BS-R bubble did not receive the late push from the lateral vortices, so its upward motion stalled (see Figure 4). At the same time, the bubble exhibited a breathing mode oscillation with a period of about 50 Myr, which is similar to the natural, Brunt-Väisälä period ($\sqrt{h/|g|} \sim 40\text{Myr}$). Figure 10 illustrates the density evolution of model BS-R, which can be compared to that of model BS_h in Figure 9. The velocity fields at $t = 150$ Myr can be compared for the two models in Figure 6.

As one final illustration of the influences of magnetic field geometry we also show in Figure 10 the density evolution of model OS. In this model the ambient magnetic field was tilted, obliquely at a 45 degree angle with respect to gravity. Absent distortions around the bubble inflation region, the ambient field would have been a uniform $5 \mu\text{G}$, pointing down and to the right. Thus, it was comparable in strength to the BM simulations in the bubble inflation region, but to the BS simulations where the bubble was found at 150 Myr. The evolution was something of a hybrid between the two classes, with an added feature due to the obliquity of the field. The bubble was initially subject to both R-T and K-H instabilities. An R-T finger briefly began to develop on top of the bubble (barely visible at $t = 12.5$ Myr in Figure 10, but it was disrupted by the lateral stresses soon imposed on the bubble by the external field. This inhibited the fragmentation process that destroyed the bubbles formed in regions of similar magnetic field strength for both horizontal and vertical field geometries. Although the bubble became highly turbulent it remained intact to the end of the simulation.

3.2.2. Continuous Inflation

All the simulations discussed above involved bubble inflation periods that were short compared to the time required for the bubble to rise through a scale height in the ICM. Our simulations suggest that so long as this condition is satisfied the subsequent evolution will be qualitatively independent of the inflation period. This conclusion is apparent from the qualitative similarities between our results discussed so far and from the simulations of R04, which used only preformed bubbles. For our ICM and bubble characteristics the critical inflation timescale is about 20 Myr. Brüggén *et al.* (2002) and Brüggén & Kaiser (2002)

presented results of hydrodynamical simulations in which a bubble inflation mechanism similar to ours was kept constant. Their unmagnetized, buoyant plasma developed flocculent plumes, so were rather different from the briefly inflated MHD bubbles discussed above or the preformed MHD bubbles simulated by R04.

In order to investigate the MHD properties of continuously inflated bubbles we carried out two simulations, BS-C and BW-C, described in Table 1. We found qualitatively similar structures to the HD plumes of Brüggén & Kaiser (2002) for our constantly inflated MHD bubbles, as illustrated in Figure 11. As pointed out in §3.1, the continuously inflated hot bubble formed a de Laval nozzle about one scale height above the inflation region, with mildly supersonic flows ($M \sim 1.1$) inflating the bubble body at higher altitudes. The plume was highly unstable to bending modes (in 2D, planar geometry), so that flows internal to the bubble, while subsonic, were chaotic with speeds several times c_{sI} . The bubble shown, BS-C, was formed in the same ICM as bubble BS_h, discussed above. The ICM was given an initial $\beta_I = 120$. The bubble was largely stable to disruptive R-T and K-H instabilities, like others with the same ambient magnetic field. As before, the ambient magnetic field was pulled up with the bubble and became roughly as strong along the bubble perimeter as it was in the BS_h simulation. Because of the strong and chaotic internal circulations within the bubble, the bubble magnetic field became highly filamented, but generally weak, due to magnetic reconnection.

We also carried out an analogous simulation, BW-C, with continuous inflation, but with the same weak magnetic field conditions as BW ($\beta_I = 75550$). This bubble remained essentially hydrodynamical until the end of the simulation, when it crossed the upper grid boundary. On the other hand, its evolution was qualitatively very similar to the B5-C bubble, except that R-T and K-H instabilities caused the bubble boundary to become very flocculent. Unlike the “free-floating” bubble BW, however, the Alfvén speed nowhere became comparable to the flow speeds along the bubble boundaries, or within the strong, internal bubble circulations. Also, in this case the flows above the de Laval nozzle reached Mach numbers approaching $M = 2$, leading to an intermittent terminal shock where the rising plume entered the bubble, as well as weak shocks within the bubble itself.

4. Summary and Conclusions

We have carried out an extensive set of 2D MHD simulations of hot buoyant MHD bubbles in a realistic ICM. Our bubbles were inflated over a finite time near the base of the ICM from a region of circular cross section and with uniform gas pressure and density and a circumferential magnetic field initially isolated from the ICM magnetic field. The

ICM magnetic fields covered a range of strengths and geometries. The simulations support the basic findings of previous analytic studies and 2D simulations and add substantial new insights. As expected from previous work, absent or very weak fields permit development of R-T and K-H instabilities, so that bubbles fragment quickly upon release into the ICM. On the other hand, as expected, moderately strong ICM magnetic fields of a few μG can stabilize R-T and K-H instabilities along the surfaces of the bubbles as they start to rise. Such bubbles remain intact as they rise through several scale heights in the ICM. Magnetic flux from the ICM is pulled up and over the rising bubble while being wrapped into vortices that form along the sides and in the wake of the bubbles. Those motions stretch and strengthen the ambient field, so that its role becomes more important as the bubbles evolve. Even though the initial magnetic pressures in our simulated environments were all less than 1% of the ambient gas pressure and the Alfvén speeds at least an order of magnitude less than the sound speeds, the magnetic pressure surrounding the bubbles can become a significant fraction of the gas pressure and the Alfvén speed comparable to the ICM sound speed and bulk flow speeds. Magnetic tension from the field draped over the bubbles can then help retard their upward movement and influence the morphology of the bubbles. Following their amplification around a bubble, even very weak ambient magnetic fields (less than a μG) eventually add stability to the bubbles or their fragments.

In addition our simulations show that the geometry of the field and the field topology at the interface between the bubble and the ICM play significant roles in the evolution of the bubbles and their fragments. For instance, we find sometimes strongly different behaviors arising, depending on whether the initial bubble and ICM fields were parallel or anti-parallel on the bubble top. In particular, anti-parallel fields there tend to reconnect, the reducing field strengths and their ability to inhibit disruptive instabilities. The orientation of the ICM field with respect to the direction of gravity also is significant. It is already well-known in 2D models that magnetic fields orthogonal to the computational plane have limited effect, since they contribute only a pressure force. Previous simulations have demonstrated differences between vertical and horizontal ICM fields. Vertical fields have limited influence on initial bubble stability, but can help confine its lateral expansion, while horizontal fields influence both behaviors. We looked, in addition, at the evolution of bubbles in oblique magnetic fields. Their roles are more comparable to those of horizontal fields in that they inhibit initial instabilities at a reduced level compared to a horizontal field of similar strength, since field lines become draped around a rising bubble. On the other hand, the Maxwell stresses induced in this situation are decidedly oblique as well, so they contribute to shearing motions within the rising bubbles that can help disrupt the nonlinear R-T fingers that do form.

The dynamical roles of the magnetic fields internal to the bubbles are more complex. Strong internal fields parallel to the boundary can play similar roles to the external field, of

course. Such fields can develop in response to vortices driven by differential and time varying buoyancy within our bubbles. In general, rising bubbles are subject to strong, varying and irregular stresses, so in many cases they develop internal circulations with speeds approaching the upward velocity of the bubble, unless the magnetic fields are strong enough to inhibit them; that is, unless the Alfvénic Mach number of the flows is relatively small. The internal motions can lead to locally strong fields where they are stretched, but they also lead to substantial field annihilation inside vortices. Consequently, the growth of total magnetic energy inside the bubbles is generally modest and irregular.

ICM gas and magnetic fields are, of course, dredged up in the bubble wakes in response to vortical flows that developed behind the bubbles. The history of those motions reflects the rising motions of the bubbles themselves. The upward velocities of our simulated bubbles are well-described by simple terminal velocity models balancing buoyancy against ram pressure drag with a constant drag coefficient appropriate to a blunt object. During the inflation process the terminal bubble velocities typically increase over time, since they rapidly displace more and more dense, ICM material. On the other hand, once inflation ends, our bubble terminal velocities generally decrease, due to the weakened gravity at higher altitudes. This effect, which seems very likely to apply in most real clusters, has a significant effect on the subsequent evolution of the bubbles. As a bubble decelerates, its wake vortices weaken and separate. In response a return flow develops in the ICM below the bubble that carries magnetic flux with it. In our 2D geometry a thin current sheet forms between oppositely directed fields. In addition, as the bubble decelerates the gravitational and Reynolds stresses that contribute to instability development are reduced. Hence, remaining bubble fragments are able to relax, and any surrounding amplified fields formed during earlier motions are also more effective in bubble stabilization.

We also explored the influence of varying the length of time over which the bubble is inflated. While short inflation periods produce behaviors similar to those of preformed bubbles, inflation over long periods leads to mushroom-capped rising plumes with internal supersonic motions and, in some cases, intermittent internal shocks. The transition between these behaviors depends on whether the bubble inflation is less than or greater than the time for buoyant material to rise through an ICM scale height above the inflation region. Since buoyant velocities are a significant fraction of the ICM sound speed, the critical inflation period is of the order of the ICM sound crossing time.

4.1. Astrophysical Implications

Several conclusions that are relevant to the formation and evolution of relic radio bubbles in clusters of galaxies can be drawn from these MHD simulations. Some of these are quite straightforward, while others are more complex or will require additional effort for their complete understanding. However, the principal points of astrophysical interest are as follows:

1) First and foremost, it is now very clear that intracluster magnetic fields that are initially dynamically unimportant can stabilize the relic radio bubbles against disruption by surface instabilities in the form of Rayleigh-Taylor and Kelvin-Helmholtz processes. Though there is currently some uncertainty in the exact values for many ICM magnetic fields (e.g., Carilli & Taylor 2002, Taylor et al. 2002, Rudnick & Blundell 2003), there is broad agreement that fields of $1 - 10\mu\text{G}$ are most likely. The resulting values of β for the ICM then lie in the range of a few tens to a few thousand, depending on the richness of the cluster and the location within the cluster. For such values of β the present calculations then show, in agreement with previous estimates, that the radio bubbles are stabilized against disruption.

2) A second and related conclusion involves the buoyant risetimes of the bubbles. These times have been estimated by Birzan et al. (2004) from the observational data to lie in the range from a few tens of millions of years to over 10^8 years, and a similar value of $\sim 10^8$ yr was obtained by Churazov et al. (2001). The calculations presented here, which include the inflation of the bubbles and realistic ICM and gravity conditions, are consistent with these estimates. A particular feature of interest in the dynamical history of the bubbles is the deceleration they experience and the role played by the magnetic field in this process, as described in Section 3. It would be of great interest in determining the ultimate fate of relic radio bubbles to follow their late time evolution in the ICM; this calculation will have to await a treatment in three dimensions.

3) A key issue in many observational and theoretical discussions of relic radio bubbles is their potential role in reheating cluster cooling flows, either by direct injection of energy or by mixing regions of the ICM that are at different temperatures. These simulations provide strong evidence of mixing and lifting of the ICM, together with mixing of the bubble material with the ICM. The location of these mixing regions can be along the sides of the bubble, in the bubble wake, and even along the top surface of the bubble. However, as discussed in Section 3, the amount of lifting and mixing is a strong function of the ICM, β and the relative orientation of the ICM and bubble magnetic fields. Magnetic field reconnection plays an important role in mediating this mixing process, and it emphasizes the need for an MHD treatment. In general, mixing and lifting is most pronounced in the wake of those bubbles that more closely resemble the observational data; i.e., for those bubbles with

stable geometries and relatively low values of β_I . At present it is not possible to provide a quantitative estimate of the overall mixing and lifting in the ICM from bubble evolution due to the limitations of the overall simulation volume, as discussed at the end of Section 3.1. Thus, while relic radio bubbles clearly contribute to reheating of the ICM, a quantitative assessment of this effect requires additional, carefully designed calculations.

4) The discussion of bubble dynamics in Section 3.2 also illustrates the importance of the interior dynamics and magnetic field structure of the bubbles in determining their interaction with the ICM. The bubbles simulated here have very simple properties; they are filled with hot, rarefied gas and have well defined field geometries. Yet, the subsequent evolution of their interior structure is complex, and it is hoped that future three-dimensional simulations will provide enough detail that inferences can be drawn about the internal composition of the bubble when comparisons are made with observations. This is a question of particular interest for two reasons. First, the observational data seem to show that the internal energy of the bubbles exceeds their minimum equipartition energy obtained from radio data by factors of 10 or more (McNamara et al. 2002, Birzan et al. 2004), and second, the particle content of radio jets is still unknown and remains one of the critical outstanding problems in this field. Hence, any insights into the particle content of the radio bubbles would be of great interest.

4.2. Future Work

A full understanding of MHD influences on the dynamics of buoyant bubbles in cluster media must await high resolution 3D MHD studies. We can, however, anticipate some of the important similarities and differences. Two important limitations of 2D flows may be important to keep in mind. First, there is no vortex stretching in 2D flows, which in 3D leads to significant strengthening of flux ropes. Thus, in 3D we may expect more intense local field amplification in complex flow regions. Our 3D MHD simulations of light, supersonic jets penetrating ICMs are consistent with that expectation (*e.g.*, Tregillis *et al.* 2001; O’Neill 2004), as are comparisons between our 2D and 3D simulations of the MHD K-H instability (*e.g.*, Jones *et al.* (1997); Ryu *et al.* (2000)). On the other hand, the relative global magnetic field enhancements seen in the 3D jet simulations are once again modest and qualitatively consistent with our results here in an admittedly somewhat different flow. Both, however, are driven flows that have generally chaotic behaviors.

One of the dominant MHD behaviors seen in the present 2D MHD simulations is the formation of dynamically strong field regions on the leading surface of the rising bubbles. Analogous features have been reported in 2D MHD simulations of fast, dense clouds moving

through magnetized media (*e.g.*, Miniati *et al.* (1999)). One possible difference in a 3D flow is the possibility that the magnetic flux will 'slide' off the top of the rising bubble. Unless the bubble is magnetically supported, that behavior is unlikely, however, as illustrated in the 3D MHD moving cloud simulations of Gregori *et al.* (1999). They found that magnetic flux of the ambient medium tends to become trapped in surface irregularities of the cloud, so that it is indeed stretched around the perimeter. Depending on the local field geometry and coherence length the dynamical outcome of that behavior is not clear, however. While it stabilizes K-H instabilities with wave vectors parallel to the field it does not do so in orthogonal directions. That behavior requires full 3D simulation to be understood.

This work was supported at the University of Minnesota by NSF grant AST03-07600 and by the University of Minnesota Supercomputing Institute. The National Optical Astronomy Observatory is operated by AURA Inc. under a cooperative agreement with the National Science Foundation. Portions of this work were performed during the 2004 astrophysics program at the Aspen Center for Physics. We thank the referee for constructive comments on improving the manuscript.

REFERENCES

- Birzan, L., David, L.P., McNamara, B.R., Wise, M.W., Nulsen, P.E.J., 2004, *ApJ*, 607, 800
- Blanton, E. L., Sarazin, C. L., McNamara, B. R. & Clarke, T. E. 2004, *ApJ*, 612, 817
- Böhringer, H., Voges, W., Fabian, A.C., Edge, A.C., Neumann, D.M., 1993, *MNRAS*, 264, L25
- Brüggen, M., Kaiser, C., 2001, *MNRAS*, 325, 676
- Brüggen, M., Kaiser, C., 2002, *Nature*, 418, 301
- Brüggen, M., Kaiser, C., Churazov, E., Ensslin, T., 2002, *MNRAS*, 331, 545
- Carilli, C.L., Taylor, G.B., 2002, *Ann Rev Ast & Ap*, 40, 319
- Celotti, A., Fabian, A.C., 1993, *MNRAS*, 264, 228
- Chandrasekhar, S. 1961, *Hydrodynamic and Hydromagnetic Stability*. Oxford, Clarendon Press, Ch 10
- Churazov, E., Brüggen, M., Kaiser, C., Böhringer, H., Forman, W., 2001, *ApJ*, 554, 261

- De Young, D.S., 1992, *ApJ*, 386, 464
- De Young, D.S., 2002, *The Physics of Extragalactic Radio Sources*. University of Chicago Press, Chicago
- De Young, D.S., 2003, *MNRAS*, 343, 719
- Eilek, J.A., Melrose, D.B., Walker, M.A., 1997, *ApJ*, 483, 282
- Fabian, A.C., 1994, *Ann Rev Ast & Ap*, 32, 277
- Fabian, A.C. et al., 2000, *MNRAS*, 318, L65
- Fabian, A.C., Celotti, A., Blundell, K.M., Kassim, N.E., Perley, R.A., 2002 *MNRAS*, 331, 369
- Fabian, A.C., et al., 2003 *MNRAS*, 344, L43
- Fujita, Y., Sarazin, C. L., Kempner, J. C., Rudnick, L., Slee, O. B., Roy, A. L., Andernach, H. & Ehle, M. 2002, *ApJ*, 575, 764
- Gregori, G., Miniati, F., Ryu, D. & Jones, T. W. 1999, *ApJ*, 527, 113
- Harris, D.E., Carilli, C., Perley, R.A., 1994, *Nature*, 367, 713
- Jones, T. W., Ryu, D. & Tregillis, I. L. 1996, *ApJ*, 473, 365
- Jones, T. W., Gaalaas, J. B., Ryu, D. & Frank, A. 1997, *ApJ*, 482, 230
- Kaiser, C.R., Cotter, G., 2002, *MNRAS*, 336, 649
- Kempner, J. C., Blanton, E. L., Clarke, T. E., Ensslin, T. A., Johnston-Hollitt, M. & Rudnick, L. 2003, *astro-ph/0310263*
- Lane, W. M., Clarke, T. E., Taylor, G. B., Perley, R. A. & Kassim, N. E. 2004, *AJ*, 127, 48
- Lee, H., Ryu, D., Kim, J., Jones, T. W. & Balsara, D. 2003, *ApJ*, 594, 627
- Mazzotta, P., Kaastra, J. S., Paerels, F. B., Ferrigno, C., Colafrancesco, S., Mewe, R. & Forman, W. R. 2002, *ApJ*, 567, L37
- McNamara, B.R., 2002a, in "X-Rays at Sharp Focus", eds. S.Vrtilek, E. Schlegel, ASP Conf. Series, Vol 262, p351
- McNamara, B.R., 2002b, private communication.

- McNamara, B.R. et al., 2001, ApJ, 562, L149
- Miniati, F., Jones, T. W. & Ryu, D. 1999, ApJ, 517, 242
- Nulsen, P.E.J., et al., 2002, ApJ, 568, 163
- O’Neill, S., Tregillis, I. L., Jones, T. W. & Ryu, D. 2004, preprint
- Orszag, S.A., 1970, J. Fl. Mech, 41, 363
- Reynolds, C.S., Heinz, S., Begelman, M., 2002, MNRAS, 332, 271
- Robinson, K., *et al.* 2004, ApJ, 601, 621
- Roettiger, K., Burns, J. O. & Stone, J. M. 1999, ApJ, 518, 603
- Ryu, D., Jones, T. W. & Frank, A. 1995, ApJ, 452, 785
- Ryu, D., Jones, T. W. & Frank, A. 2000, ApJ, 545, 475
- Shore, S.N., 1992, An Introduction to Astrophysical Hydrodynamics. Academic Press, New York
- Slee, O., Roy, A., Murgia, M., Andernach, H., Ehle, M. 2001, AJ, 122, 1172
- Smith, M. D., Smarr, L., Norman, M. L. & Wilson, J. R. 1983, ApJ, 264, 432
- Soker, N., Blanton, E. L., Sarazin, C.L., 2002, ApJ, 573, 533
- Taylor, G.B., Fabian, A.C., Allen, S.W., 2002, MNRAS, 334, 769
- Tregillis, I. L., Jones, T. W. & Ryu, D. 2001, ApJ, 557, 475
- Tribble, P.C., 1994, MNRAS, 269, 110
- Young, A, Rudnick, L., Andernach, H., Kassim, N., Roy, A. & Slee, B. 2004 (preprint).

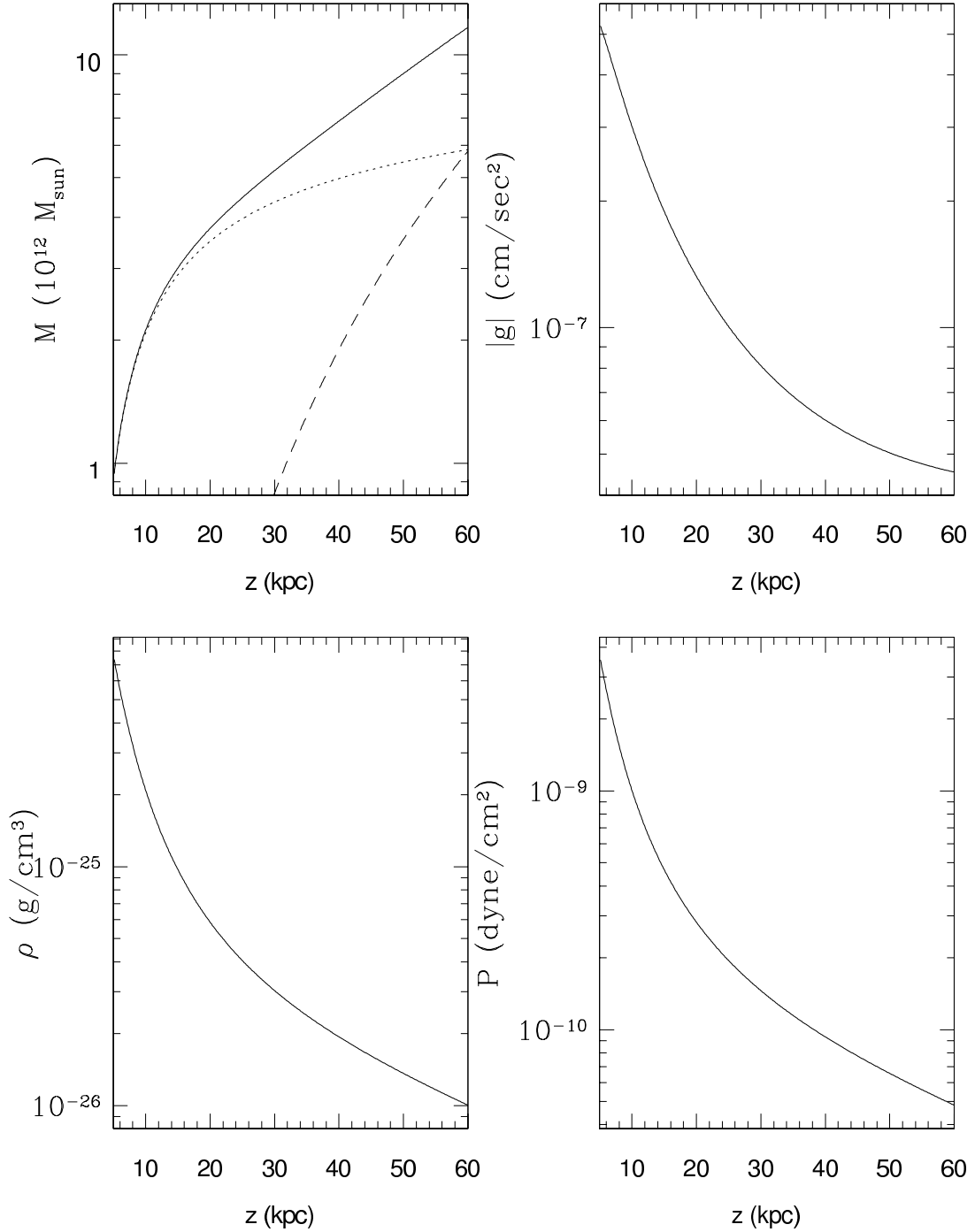


Fig. 1.— Initial environment of the bubble simulations. Top left: Gravitational mass as a function of radius from the core – total (solid), galaxy (dotted), cluster (dashed). Top right: gravitational acceleration, Lower left: gas density, Lower right: gas pressure. Distance from the mass center is represented by z to reflect the symmetry of the MHD simulations.

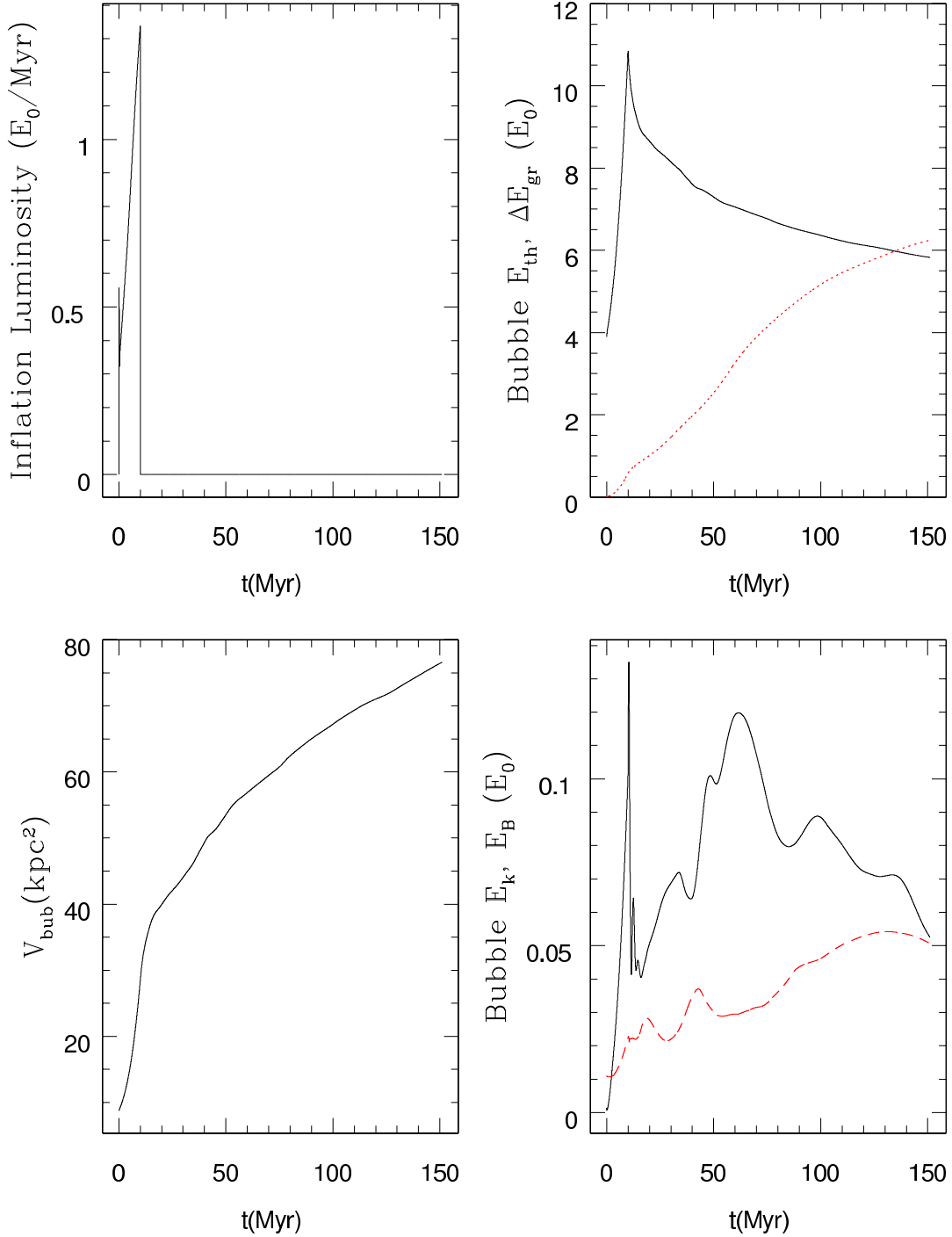


Fig. 2.— Energetics of the bubble in model BM_h . Top: left- Total 2D energy flux through the boundary of the bubble inflation region; right- Bubble thermal energy (solid line) and net change in gravitational energy (dotted line). Bottom: left-Bubble 2D “volume”; right- Bubble kinetic energy (solid line) and magnetic energy (dashed line). Energy units are $E_0 = 5.5 \times 10^{55}$ erg.

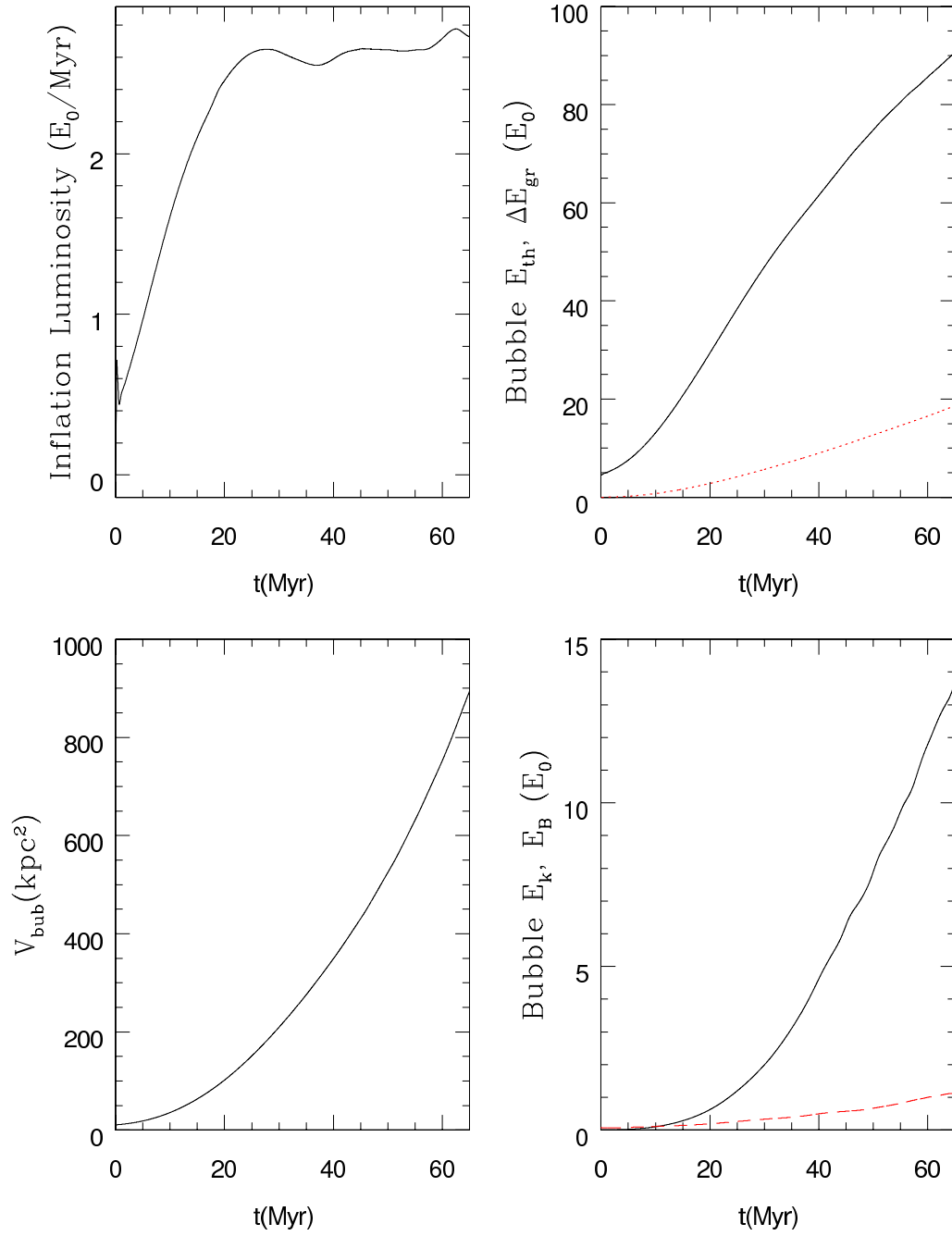


Fig. 3.— Same as Figure 2, except for model BS-C.

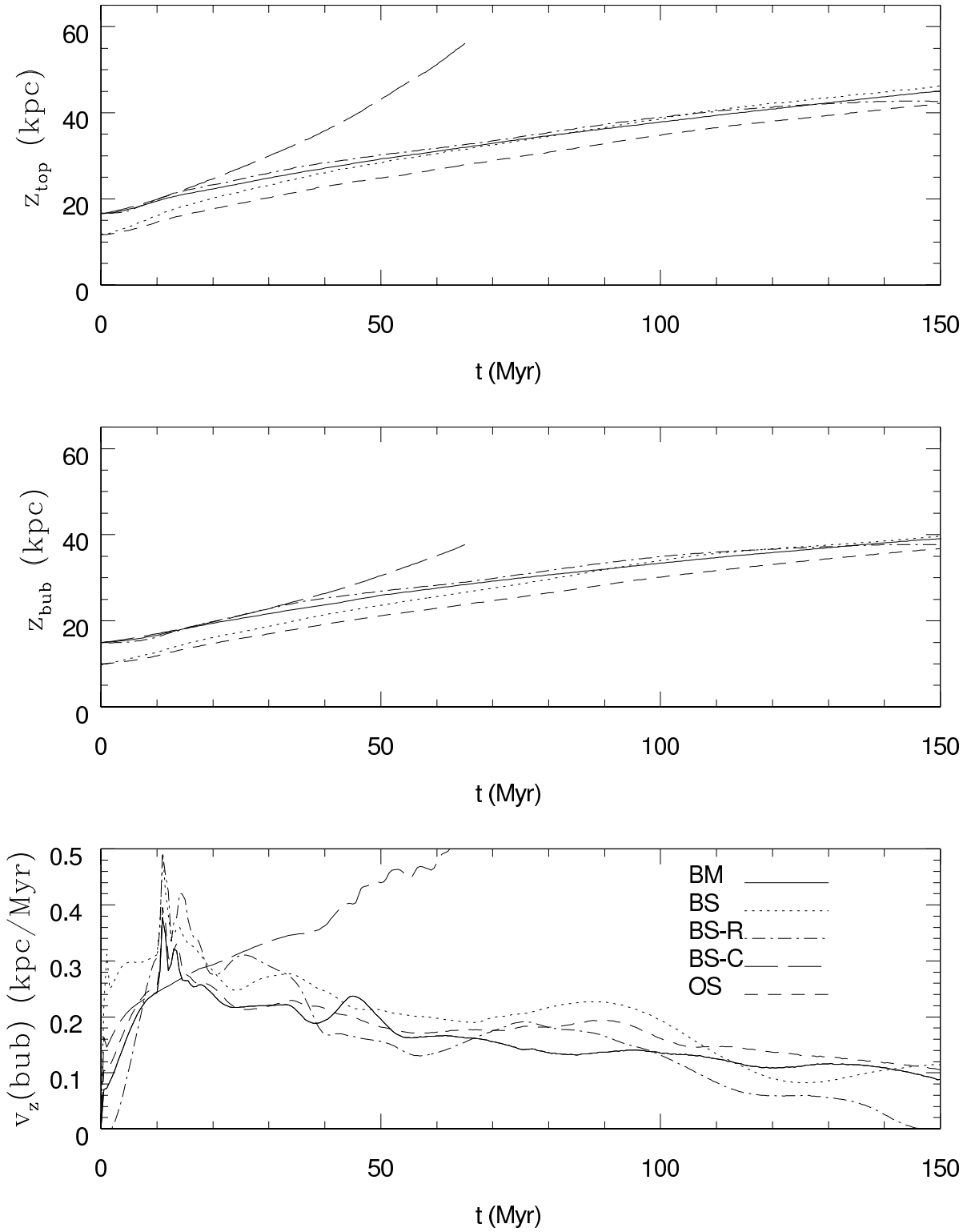


Fig. 4.— Upward motions of several model bubbles as labelled. Top: position of the top of the bubble; Middle: position of the mean height of the bubble; Bottom: velocity of the mean bubble height.

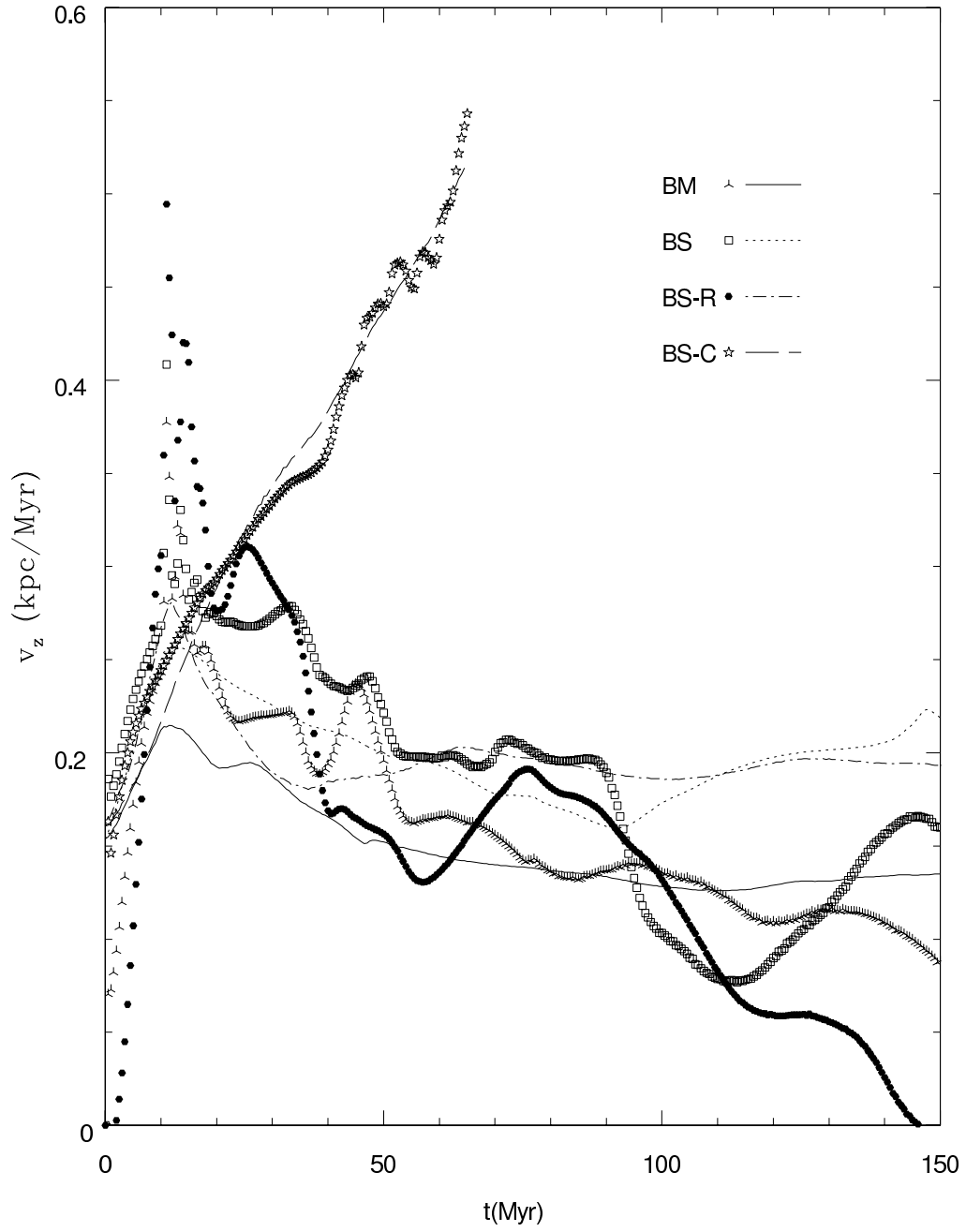


Fig. 5.— Upward velocity of three model bubbles (points as labelled) compared to a semi-analytic buoyancy model as described in the text (equation 5).

See f6.jpg

High resolution image available at <http://www.msi.umn.edu/Projects/twj/bubbles/f6.eps>

Fig. 6.— Velocity vectors overlaid on bubble mass-fraction (C_f) contours at $t = 150\text{Myr}$ for the BW (upper left), BM_h (Upper right), BS_h (lower left) and BS-R (lower right) models. See the electronic version of the Journal for a color version of this figure.

See f7.jpg

High resolution image available at <http://www.msi.umn.edu/Projects/twj/bubbles/f7.eps>

Fig. 7.— Snapshots from the evolution of the magnetic pressure (P_b) and gas density (ρ) in the model BW ($\beta_I \approx 7.6 \times 10^4$). Images apply a logarithmic color bar with high values represented by high tones. The magnetic pressure spans six decades, with a peak value $P_{b_{peak}} \approx 10^{-12} \text{ dyne/cm}^2$ ($B_{peak} \approx 5\mu\text{G}$), while the gas density spans 2.6 decades, with $\rho_{peak} \approx 7.6 \times 10^{-25} \text{ g/cm}^{-3}$. See the electronic edition of the Journal for a color version of this figure.

See f8.jpg

High resolution image available at <http://www.msi.umn.edu/Projects/twj/bubbles/f8.eps>

Fig. 8.— Same as Figure 7, but for model BM_h ($\beta_I \approx 3 \times 10^3$). The peak magnetic field reaches about $20 \mu\text{G}$.

See f9.jpg

High resolution image available at <http://www.msi.umn.edu/Projects/twj/bubbles/f9.eps>

Fig. 9.— Same as Figure 8, but for model BS_h ($\beta_I \approx 120$). The peak magnetic field reaches about $40 \mu\text{G}$.

See f10.jpg

High resolution image available at <http://www.msi.umn.edu/Projects/twj/bubbles/f10.eps>

Fig. 10.— Snapshots from the density evolution of models BS-R and OS, showing some of the dynamical influences of magnetic field geometry. Display characteristics are the same as Figure 7. See the electronic edition of the Journal for a color version of this figure.

See f11.jpg

High resolution image available at <http://www.msi.umn.edu/Projects/twj/bubbles/f11.eps>

Fig. 11.— Magnetic pressure and density evolution for model BS-C, which is the same as BS, except that $t_i = t_e$. See the electronic version of the Journal for a color version of this figure.

Table 1. Summary of Models Discussed

Model ^a	Resolution ^b	Ambient Field Geometry ^{c d}	β_I^c	B_I^c ^e μG	B_{bub}^f ^g μG	t_i Myr	t_e Myr
BW	512×512	hb	75550	0.2	2(CCW)	10	150
BW-C	512×512	hb	75550	0.2	2(CCW)	75	75
BM	512×512	hb	3000	1	10(CCW)	10	150
BM _h	1024×1024	hb	3000	1	10(CCW)	10	150
BM-R	512×512	hb	120	1	10(CW)	10	150
BS	512×512	hb	120	5	50(CCW)	10	150
BS _h	1024×1024	hb	120	5	50(CCW)	10	150
BS-R	512×512	hb	120	5	50(CW)	10	150
BS-C	512×512	hb	120	5	50(CCW)	65	65
OS	512×512	ou	50 - 3000	5	10(CCW)	10	110

^aSee note below for key to model labels.

^bAll simulations used a Cartesian domain $y = [-27.5, 27.5]$ kpc, $z = [5, 60]$ kpc.

^cMeasured away from bubble influence

^dh = horizontal ($\phi_0 = 0^\circ$), o = oblique ($\phi_0 = -45^\circ$), v = vertical ($\phi_0 = 90^\circ$); b = constant β_I , u = “uniform”

^e $z = 30$ kpc

^fMaximum value measured at $r = r'_b$ during bubble inflation

^gCCW = counterclockwise field orientation; CW = clockwise (or “reversed”) field orientation

Note. — The primary two letter model designation indicates the geometry of the ICM magnetic field (column 3) followed by a qualitative indicator of relative field strength; weak (W), medium (M) or strong (S). The two high resolution simulations are additionally marked by the subscript h. Continuous injection models are tagged with “-C”, while those with the bubble magnetic field reversed (CW) have the designation “-R”.

This figure "f6.jpg" is available in "jpg" format from:

<http://arxiv.org/ps/astro-ph/0502146v1>

This figure "f7.jpg" is available in "jpg" format from:

<http://arxiv.org/ps/astro-ph/0502146v1>

This figure "f8.jpg" is available in "jpg" format from:

<http://arxiv.org/ps/astro-ph/0502146v1>

This figure "f9.jpg" is available in "jpg" format from:

<http://arxiv.org/ps/astro-ph/0502146v1>

This figure "f10.jpg" is available in "jpg" format from:

<http://arxiv.org/ps/astro-ph/0502146v1>

This figure "f11.jpg" is available in "jpg" format from:

<http://arxiv.org/ps/astro-ph/0502146v1>